

A High-Order Discretization Scheme for Surface Integral Equations for Analyzing the Electroencephalography Forward Problem

Rui Chen, Member, IEEE, Viviana Giunzioni, Member, IEEE, Adrien Merlini, Senior Member, IEEE, and Francesco P. Andriulli, Fellow, IEEE

Abstract—A Nyström-based high-order (HO) discretization scheme for surface integral equations (SIEs) for analyzing the electroencephalography (EEG) forward problem is proposed in this work. We use HO surface elements and interpolation functions for the discretization of the interfaces of the head volume and the unknowns on the elements, respectively. The advantage of this work over existing isoparametric HO discretization schemes resides in the fact that the interpolation points are different from the mesh nodes, allowing for the flexible manipulation of the order of the basis functions without regenerating the mesh of the interfaces. Moreover, the interpolation points are chosen from the quadrature rules with the same number of points on the elements simplifying the numerical computation of the surface integrals for the far-interaction case. In this contribution, we extend the implementation of the HO discretization scheme to the double-layer and the adjoint double-layer formulations, as well as to the isolated-skull-approach for the double-layer formulation and to the indirect adjoint double-layer formulation, employed to improve the solution accuracy in case of high conductivity contrast models, which requires the development of different techniques for the singularity treatment. Numerical experiments are presented to demonstrate the accuracy, flexibility, and efficiency of the proposed scheme for the four SIEs for analyzing the EEG forward problem.

Keywords—EEG forward problem, high-order discretization, Nyström method, surface integral equation.

I. Introduction

ELCTROENCEPHALOGRAPHY (EEG) is one of the widely used non-invasive neurophysiological techniques for functional neuroimaging that aims to determine

This work was supported in part by the National Natural Science Foundation of China (NSFC) under Grant 62201264 and Grant 62331016; in part by the Fundamental Research Funds for the Central Universities under Grant 30924010207; in part by the Fund Program for the Scientific Activities of Selected Returned Overseas Professionals in Shanxi Province under Grant 20240063; in part by European Innovation Council (EIC) under Grant 101046748; in part by European Union-Next Generation EU under Grant CUP E13C22000990001; and in part by the Labex CominLabs Excellence Laboratory under Grant ANR-10-LABX-07-01. (Corresponding author: Rui Chen.)

Rui Chen is with the School of Microelectronics, Nanjing University of Science and Technology, Nanjing 210094, China (e-mail: rui.chen@njjust.edu.cn).

Viviana Giunzioni and Francesco P. Andriulli are with the Department of Electronics and Telecommunications, Politecnico di Torino, 10129 Turin, Italy (e-mail: viviana.giunzioni@polito.it; francesco.andriulli@polito.it).

Adrien Merlini is with the Department of Microwave, IMT Atlantique, 29238 Brest, France (e-mail: adrien.merlini@imt-atlantique.fr).

location, intensity, and orientation of the activity of the neural source in the head volume [1]. Although EEG-based neuroimaging has good temporal resolution, its spatial resolution needs further improvement [2].

EEG-based imaging techniques characterize the neural activity in the head volume from the electric potential directly measured at the electrodes placed on the surface of the scalp, which is termed as “EEG inverse problem” [3]. To analyze the EEG inverse problem, the solution of the EEG forward problem, i.e., the evaluation of the electric potential on the scalp surface with the given hypothetical neural source and electrical property of the biological tissues in the head volume, is required [4]. Since the accuracy of the analysis of the EEG inverse problem depends on that of the solution of the EEG forward problem [5], we could improve the spatial resolution of EEG via the later.

In the last decades, many numerical methods have been developed for the solution of the EEG forward problem. Two kinds of the commonly used methods are differential equation- and surface integral equation (SIE)-based methods [6]–[22]. Compared with the differential equation-based methods [6]–[9], the SIE-based methods [10]–[22] remove the need of (artificial) absorbing boundary conditions and use surface elements instead of volumetric elements for the object discretization, resulting in fewer unknowns [10].

The SIE-based methods solve SIEs enforced on the interfaces between the neighboring biological tissue layers in the head volume for the unknowns on the interfaces [11]. To improve the accuracy of the solution of the EEG forward problem, one could improve that of the discretization of the interfaces and unknowns [12]. On one hand, traditionally, low-order (LO) surface elements (e.g., planar triangular patch) are usually used for the discretization of the interfaces [10]–[19]. However, as the interfaces are not regular, the use of LO surface elements introduces non-negligible geometrical error. Instead, the use high-order (HO) surface elements (e.g., curved triangular patch) improves the modeling accuracy [20]–[22]. On the other hand, traditionally, LO basis functions are usually used for the discretization of the unknowns [10]–[19]. However, the approximation accuracy is limited using LO basis functions. Instead, one could use HO basis functions to improve the approximation accuracy of the unknowns

[20]–[22].

In the past years, several works have used the HO surface elements and HO basis functions simultaneously for the discretization of SIEs for analyzing the EEG forward problem [20]–[22]. [20] used quadratically curved triangular elements for the discretization of the interfaces and quadratic interpolation functions associated with the interpolation points for the discretization of the electric potential. [21] and [22] used the HO basis functions for the discretization of the unknown on the planar, quadratic, and cubic triangular elements. [20]–[22] used the isoparametric HO discretization scheme for SIEs, i.e., the same interpolation functions are used for the definition of the surface elements and of the unknown on the elements and the mesh nodes are overlapped with the interpolation points for each element. However, it limits the flexibility of the HO discretization of SIEs. For instance, to use the higher-order basis functions, one has to first regenerate the mesh of the interfaces with the higher-order surface elements.

To address this issue, we propose a Nyström-based HO discretization scheme for SIEs for analyzing the EEG forward problem in this work. The unknowns on the HO surface elements are approximated using the HO interpolation functions associated with the interpolation points. The novelty of this work over the existing works using the isoparametric HO discretization scheme is “threefold”:

- 1) The interpolation points are located on the elements instead of the boundary of the elements. Since the interpolation points are independent of the mesh nodes, we could flexibly manipulate the order of the basis functions without regenerating the mesh of the interfaces.
- 2) The interpolation points are chosen from the quadrature rules with the same number of points on the elements. The numerical computation of the surface integrals can be simplified for the far-interaction case.
- 3) We extend the implementation of the HO discretization scheme to the double-layer approach and the adjoint double-layer approach, as well as to the isolated skull approach for the double-layer formulation and to the indirect adjoint double-layer approach for analyzing the EEG forward problem, which needs the development of different techniques for the singularity treatment.

Note that, even though the Nyström-based methods have been reported in electromagnetics [23]–[25] and acoustics [26]–[28], to the best of the authors’ knowledge, the Nyström-based HO discretization scheme has never been used for SIEs for analyzing the EEG forward problem. A preliminary conference version of this work is presented in [29] while this paper presents more implementation details.

II. Formulation

A. SIEs for the EEG Forward Problem

When using SIEs for analyzing the EEG forward problem, the head volume Ω is usually modeled as a piecewise,

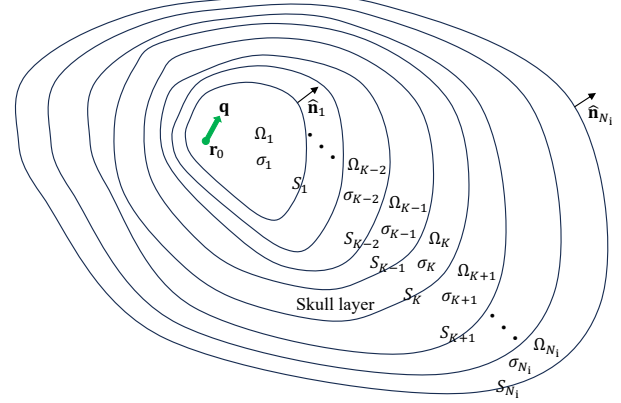


Fig. 1. The head volume model.

homogeneous, and multilayered conductor (as seen in Fig. 1). The layers (representing the biological tissues) from the inner to the outer are denoted as $\Omega_1, \Omega_2, \dots, \Omega_{N_i}$, with the constant conductivities $\sigma_1, \sigma_2, \dots, \sigma_{N_i}$, respectively. The skull layer is located in Ω_K between S_{K-1} and S_K with the conductivity σ_K . The interfaces between the neighboring layers are S_1, S_2, \dots, S_{N_i} from the inner to the outer, where the outward pointing unit normal vectors $\hat{\mathbf{n}}_1, \hat{\mathbf{n}}_2, \dots, \hat{\mathbf{n}}_{N_i}$ are defined. Note that we assume that the conductivity of the homogeneous background medium outside Ω is zero in this work.

In addition, the neural source in the head volume is often modeled as an electric current dipole for SIEs for the EEG forward problem [12]. The electric potential generated by the dipolar source in the background region is

$$V^{\text{inc}}(\mathbf{r}) = \frac{\mathbf{q} \cdot (\mathbf{r} - \mathbf{r}_0)}{4\pi|\mathbf{r} - \mathbf{r}_0|^3} \quad (1)$$

where \mathbf{q} is the dipolar moment, \mathbf{r} is the observation point, and the dipole position is assumed to be $\mathbf{r}_0 \in \Omega_1$ in this work.

In the following, four approaches are introduced for computing the electric potential $V(\mathbf{r})$ for the EEG forward problem.

- 1) Double-Layer Approach: SIE in the double-layer (DL) formulation is expressed as [12]

$$V^{\text{inc}}(\mathbf{r}) = \frac{\sigma_j + \sigma_{j+1}}{2} V(\mathbf{r}) - \sum_{i=1}^{N_i} (\sigma_{i+1} - \sigma_i) \times \\ \text{P.V.} \int_{S_i} \partial_{\mathbf{n}'} G(\mathbf{r}, \mathbf{r}') V(\mathbf{r}') d\mathbf{r}', \quad \mathbf{r} \in S_j, \quad j = 1, \dots, N_i \quad (2)$$

where \mathbf{r}' is the source point, $\partial_{\mathbf{n}'} = \hat{\mathbf{n}}'(\mathbf{r}') \cdot \nabla'$, $\hat{\mathbf{n}}'(\mathbf{r}')$ is the outward pointing unit normal vector at \mathbf{r}' , $G(\mathbf{r}, \mathbf{r}') = 1/(4\pi|\mathbf{r} - \mathbf{r}'|)$ is the Green function, and $V(\mathbf{r})$ and $V(\mathbf{r}')$ represent the electric potential at \mathbf{r} and \mathbf{r}' , respectively. Here, “P.V.” denotes the “principal value”.

2) Adjoint Double-Layer Approach: SIE in the adjoint double-layer (ADL) formulation is expressed as [12]

$$\partial_{\mathbf{n}} \left[\frac{V^{\text{inc}}(\mathbf{r})}{\sigma_1} \right] = \frac{\sigma_j + \sigma_{j+1}}{2(\sigma_{j+1} - \sigma_j)} \xi(\mathbf{r}) - \sum_{i=1}^{N_i} \text{P.V.} \int_{S_i} \partial_{\mathbf{n}} G(\mathbf{r}, \mathbf{r}') \xi(\mathbf{r}') d\mathbf{r}', \quad \mathbf{r} \in S_j, \quad j = 1, \dots, N_i \quad (3)$$

where $\partial_{\mathbf{n}} = \hat{\mathbf{n}}(\mathbf{r}) \cdot \nabla$, and $\xi(\mathbf{r})$ and $\xi(\mathbf{r}')$ represent the jump of $\partial_{\mathbf{n}} V(\mathbf{r})$ and $\partial_{\mathbf{n}} V(\mathbf{r}')$ along the direction of the outward pointing unit normal vectors at \mathbf{r} and \mathbf{r}' , respectively.

After $\xi(\mathbf{r})$ is obtained by solving (3), $V(\mathbf{r})$ can be calculated as a sum of an electric potential term for excitation and single-layer surface integral operators for correction as follows [12]

$$V(\mathbf{r}) = \frac{V^{\text{inc}}(\mathbf{r})}{\sigma_1} + \sum_{i=1}^{N_i} \int_{S_i} G(\mathbf{r}, \mathbf{r}') \xi(\mathbf{r}') d\mathbf{r}', \quad \mathbf{r} \in S_j, \quad j = 1, \dots, N_i. \quad (4)$$

3) Isolated Skull Approach for the Double-Layer Approach: The isolated skull approach (ISA) is originally developed to address the numerical inaccuracies of the DL formulation due to the low conductivity of one layer of the head volume conductor model [16]. ISA decomposes $V(\mathbf{r})$ as

$$V(\mathbf{r}) = \begin{cases} V_{\text{ISA}}(\mathbf{r}) + V_{\text{corr}}(\mathbf{r}), & \text{if } \mathbf{r} \in S_1, \dots, S_{K-1} \\ V_{\text{corr}}(\mathbf{r}), & \text{if } \mathbf{r} \in S_K, S_{K+1}, \dots, S_{N_i} \end{cases} \quad (5)$$

where $V_{\text{ISA}}(\mathbf{r})$ is the solution of an isolated model considering only the tissues under the skull layer with the surfaces S_1, S_2, \dots, S_{K-1} and $V_{\text{corr}}(\mathbf{r})$ is the correction term. Note that, $V_{\text{ISA}}(\mathbf{r}) = 0$ at $\mathbf{r} \in S_K, S_{K+1}, \dots, S_{N_i}$ for ISA.

SIE in the unknown of $V_{\text{ISA}}(\mathbf{r})$ is expressed as

$$V^{\text{inc}}(\mathbf{r}) = \frac{\sigma_j + \sigma_{j+1}}{2} V_{\text{ISA}}(\mathbf{r}) - \sum_{i=1}^{K-2} (\sigma_{i+1} - \sigma_i) \times \text{P.V.} \int_{S_i} \partial_{\mathbf{n}'} G(\mathbf{r}, \mathbf{r}') V_{\text{ISA}}(\mathbf{r}') d\mathbf{r}' + \sigma_{K-1} \times \text{P.V.} \int_{S_{K-1}} \partial_{\mathbf{n}'} G(\mathbf{r}, \mathbf{r}') V_{\text{ISA}}(\mathbf{r}') d\mathbf{r}', \quad \mathbf{r} \in S_1, \dots, S_{K-1} \quad (6)$$

and SIE in the unknown of $V_{\text{corr}}(\mathbf{r})$ is expressed as

$$V_{\text{corr}}^{\text{inc}}(\mathbf{r}) = \frac{\sigma_j + \sigma_{j+1}}{2} V_{\text{corr}}(\mathbf{r}) - \sum_{i=1}^{N_i} (\sigma_{i+1} - \sigma_i) \times \text{P.V.} \int_{S_i} \partial_{\mathbf{n}'} G(\mathbf{r}, \mathbf{r}') V_{\text{corr}}(\mathbf{r}') d\mathbf{r}', \quad \mathbf{r} \in S_1, S_2, \dots, S_{N_i} \quad (7)$$

where the expression of $V_{\text{corr}}^{\text{inc}}(\mathbf{r})$ is given by

$$V_{\text{corr}}^{\text{inc}}(\mathbf{r}) = \begin{cases} \frac{\sigma_K}{\sigma_{K-1}} V^{\text{inc}}(\mathbf{r}) + \sum_{i=1}^{K-2} \frac{\sigma_K(\sigma_{i+1} - \sigma_i)}{\sigma_{K-1}} \times \int_{S_i} \partial_{\mathbf{n}'} G(\mathbf{r}, \mathbf{r}') V_{\text{ISA}}(\mathbf{r}') d\mathbf{r}', & \text{if } \mathbf{r} \in S_K, S_{K+1}, \dots, S_{N_i} \\ \frac{\sigma_K}{\sigma_{K-1}} V^{\text{inc}}(\mathbf{r}) - \sigma_K V_{\text{ISA}}(\mathbf{r}) + \sum_{i=1}^{K-2} \frac{\sigma_K(\sigma_{i+1} - \sigma_i)}{\sigma_{K-1}} \times \int_{S_i} \partial_{\mathbf{n}'} G(\mathbf{r}, \mathbf{r}') V_{\text{ISA}}(\mathbf{r}') d\mathbf{r}', & \text{if } \mathbf{r} \in S_{K-1} \\ \frac{\sigma_K}{\sigma_{K-1}} V^{\text{inc}}(\mathbf{r}) - \frac{\sigma_K(\sigma_j + \sigma_{j+1})}{2\sigma_{K-1}} V_{\text{ISA}}(\mathbf{r}) + \sum_{i=1}^{K-2} \frac{\sigma_K(\sigma_{i+1} - \sigma_i)}{\sigma_{K-1}} \times \text{P.V.} \int_{S_i} \partial_{\mathbf{n}'} G(\mathbf{r}, \mathbf{r}') V_{\text{ISA}}(\mathbf{r}') d\mathbf{r}', & \text{if } \mathbf{r} \in S_1, \dots, S_{K-2} \end{cases} \quad (8)$$

4) Indirect Adjoint Double-Layer Approach: The indirect adjoint double-layer (IADL) formulation is originally developed to address the high conductivity ratio issue of the ADL formulation [18]. IADL writes $V(\mathbf{r})$, $\mathbf{r} \in \Omega_{N_i}$ using auxiliary sources $J_{N_i-1}(\mathbf{r})$, $\mathbf{r} \in S_{N_i-1}$ and $J_{N_i}(\mathbf{r})$, $\mathbf{r} \in S_{N_i}$ as

$$V(\mathbf{r}) = \int_{S_{N_i-1}} G(\mathbf{r}, \mathbf{r}') J_{N_i-1}(\mathbf{r}') d\mathbf{r}' + \int_{S_{N_i}} G(\mathbf{r}, \mathbf{r}') J_{N_i}(\mathbf{r}') d\mathbf{r}', \quad \mathbf{r} \in \Omega_{N_i}. \quad (9)$$

Additionally, SIEs in unknowns of $J_{N_i-1}(\mathbf{r})$ and $J_{N_i}(\mathbf{r})$ are

$$\begin{aligned} & \frac{\sigma_{N_i-1}}{\sigma_{N_i} - \sigma_{N_i-1}} \xi(\mathbf{r}) = \\ & -\frac{1}{2} J_{N_i-1}(\mathbf{r}) + \text{P.V.} \int_{S_{N_i-1}} \partial_{\mathbf{n}} G(\mathbf{r}, \mathbf{r}') J_{N_i-1}(\mathbf{r}') d\mathbf{r}' \\ & + \int_{S_{N_i}} \partial_{\mathbf{n}} G(\mathbf{r}, \mathbf{r}') J_{N_i}(\mathbf{r}') d\mathbf{r}', \quad \mathbf{r} \in S_{N_i-1}^+ \end{aligned} \quad (10)$$

$$\begin{aligned} & 0 = \frac{1}{2} J_{N_i}(\mathbf{r}) + \int_{S_{N_i-1}} \partial_{\mathbf{n}} G(\mathbf{r}, \mathbf{r}') J_{N_i-1}(\mathbf{r}') d\mathbf{r}' \\ & + \text{P.V.} \int_{S_{N_i}} \partial_{\mathbf{n}} G(\mathbf{r}, \mathbf{r}') J_{N_i}(\mathbf{r}') d\mathbf{r}', \quad \mathbf{r} \in S_{N_i}^- \end{aligned} \quad (11)$$

where $\xi(\mathbf{r})$ is the solution of (3). After the solution of (10)-(11), $V(\mathbf{r})$, $\mathbf{r} \in \Omega_{N_i}$ could be obtained using (9).

B. Discretization of SIEs

To numerically solve SIEs in Section II-A, we use the Nyström method [23] in this work. The basic implementation steps of the Nyström method are introduced as follows.

First, the interfaces of the head volume conductor model S_1, S_2, \dots, S_{N_i} are discretized using $N_p^1, N_p^2, \dots, N_p^{N_i}$ quadratically curved triangular patches, respectively, with six mesh nodes along the boundary of each patch (as seen in Fig. 2). The average length of all the meshed edges is h .

Next, the unknown $\Phi(\mathbf{r})$ of SIEs on one patch Δ_p^i can be numerically approximated using the interpolation functions associated with the interpolation points on the patch as

$$\Phi(\mathbf{r}) = \sum_{a=1}^{N_a} \{\mathbf{I}_\Phi\}_a \vartheta^{-1}(\mathbf{r}) L_a(\mathbf{r}) \quad (12)$$

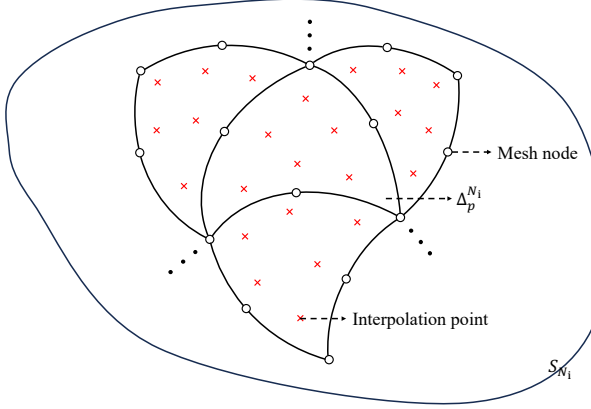


Fig. 2. An example for the discretization of S_{N_i} using the quadratically curved triangular patches with six mesh nodes along the boundary of each patch and using the 2nd order interpolation function with six interpolation points on each patch.

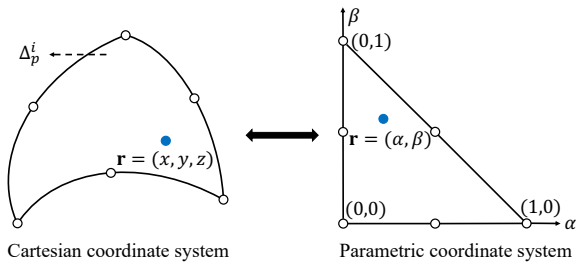


Fig. 3. The space mapping between the (x, y, z) Cartesian and (α, β) parametric coordinate systems for the p^{th} patch on S_i .

where $\Phi = \{V, \xi, V_{\text{ISA}}, V_{\text{corr}}, J_{N_i-1}, J_{N_i}\}$, N_a is the number of the interpolation points on each patch (as seen in Fig. 2), $\vartheta(\mathbf{r})$ represents the Jacobian term at \mathbf{r} resulting from the space mapping between the (x, y, z) Cartesian and (α, β) parametric coordinate systems (as seen in Fig. 3), $\{\mathbf{I}_\Phi\}_a$ is the expansion coefficient associated with the a th interpolation point on the patch, and $L_a(\mathbf{r})$, $a = 1, 2, \dots, N_a$ denotes the interpolation functions associated with the interpolation points on the patch with the property $L_a(\mathbf{r}) = 1$ when \mathbf{r} is the a th interpolation point and $L_a(\mathbf{r}) = 0$ when \mathbf{r} is the other interpolation point. Moreover, $N_a = \{1, 3, 6\}$ correspond to the $\{0, 1, 2\}$ th order interpolation function, respectively [23]. In addition, $L_a(\mathbf{r})$, $a = 1, 2, \dots, N_a$ can be obtained by solving the Lagrange polynomials-based matrix equation, e.g., when $N_a = 6$, which can be expressed as

$$\begin{bmatrix} 1 & 1 & \dots & 1 \\ \alpha_1 & \alpha_2 & \dots & \alpha_6 \\ \beta_1 & \beta_2 & \dots & \beta_6 \\ \alpha_1^2 & \alpha_2^2 & \dots & \alpha_6^2 \\ \alpha_1\beta_1 & \alpha_2\beta_2 & \dots & \alpha_6\beta_6 \\ \beta_1^2 & \beta_2^2 & \dots & \beta_6^2 \end{bmatrix} \begin{bmatrix} L_1(\mathbf{r}) \\ L_2(\mathbf{r}) \\ L_3(\mathbf{r}) \\ L_4(\mathbf{r}) \\ L_5(\mathbf{r}) \\ L_6(\mathbf{r}) \end{bmatrix} = \begin{bmatrix} 1 \\ \alpha \\ \beta \\ \alpha^2 \\ \alpha\beta \\ \beta^2 \end{bmatrix} \quad (13)$$

where (α, β) and (α_a, β_a) are coordinates of \mathbf{r} and the a th interpolation point on Δ_p^i in the parametric system, respectively.

Then, inserting the approximation of the unknowns in

(12) into the SIEs in Section II-A and point-testing the resulting equations at the observation points (chosen to be the same as the interpolation points) yields the fully discretized matrix equation systems that can be solved for the unknown expansion coefficients $\{\mathbf{I}_\Phi\}_a$. Note that we choose the N_a interpolation points on each patch on the same locations as the N_a Gaussian quadrature points on the patch, positioned according to the N_a -point Gaussian quadrature rule [30] for the Nyström method used in this work.

In the following section, the discretization of the four SIEs in Section II-A for analyzing the EEG forward problem using the Nyström method are presented.

1) DL Formulation: For the DL approach, the unknown $V(\mathbf{r})$ at $\mathbf{r} \in S_1, S_2, \dots, S_{N_i}$ is expanded as

$$V(\mathbf{r}) = \sum_{i=1}^{N_i} \sum_{p=1}^{N_p^i} \sum_{a=1}^{N_a} \{\mathbf{I}_V\}_{(a,p,i)} \vartheta^{-1}(\mathbf{r}) L_{(a,p,i)}(\mathbf{r}). \quad (14)$$

Inserting (14) into (2) and point-testing the resulting equation at the observation points $\mathbf{r}_{(b,q,j)}$, $j = 1, 2, \dots, N_i$, $q = 1, 2, \dots, N_p^j$, $b = 1, 2, \dots, N_a$ yields the matrix equation system

$$\mathbf{Z}_V \mathbf{I}_V = \mathbf{V}_V \quad (15)$$

where the entries of \mathbf{V}_V with the dimension of $N_s^V \times 1$ and \mathbf{Z}_V with the dimension of $N_s^V \times N_s^V$ are given by

$$\{\mathbf{V}_V\}_{(b,q,j)} = V^{\text{inc}}(\mathbf{r}_{(b,q,j)}) \quad (16)$$

$$\begin{aligned} \{\mathbf{Z}_V\}_{(b,q,j)(a,p,i)} &= \frac{\sigma_j + \sigma_{j+1}}{2} \vartheta^{-1}(\mathbf{r}_{(b,q,j)}) \delta_{ab} \delta_{pq} \delta_{ij} - \\ &(\sigma_{i+1} - \sigma_i) \text{P.V.} \int_{\Delta_p^i} \partial_{\mathbf{n}'} G(\mathbf{r}_{(b,q,j)}, \mathbf{r}') \vartheta^{-1}(\mathbf{r}') L_{(a,p,i)}(\mathbf{r}') d\mathbf{r}' \end{aligned} \quad (17)$$

where $N_s^V = N_a \sum_{i=1}^{N_i} N_p^i$, $\delta_{ab} = 1$ for $a = b$ and $\delta_{ab} = 0$ for $a \neq b$, Δ_p^i denotes the p th quadratically curved triangular patch on S_i . After the solution of (15) for \mathbf{I}_V , $V(\mathbf{r})$ at \mathbf{r} on one patch of S_1, \dots, S_{N_i} can be obtained using (12).

2) ADL Formulation: For the ADL approach, the unknown $\xi(\mathbf{r})$ at $\mathbf{r} \in S_1, S_2, \dots, S_{N_i}$ is expanded as

$$\xi(\mathbf{r}) = \sum_{i=1}^{N_i} \sum_{p=1}^{N_p^i} \sum_{a=1}^{N_a} \{\mathbf{I}_\xi\}_{(a,p,i)} \vartheta^{-1}(\mathbf{r}) L_{(a,p,i)}(\mathbf{r}). \quad (18)$$

Inserting (18) into (3) and point-testing the resulting equation at the observation points $\mathbf{r}_{(b,q,j)}$, $j = 1, 2, \dots, N_i$, $q = 1, 2, \dots, N_p^j$, $b = 1, 2, \dots, N_a$ yields the matrix equation system

$$\mathbf{Z}_\xi \mathbf{I}_\xi = \mathbf{V}_\xi \quad (19)$$

where the entries of \mathbf{V}_ξ in the dimension of $N_s^\xi \times 1$ and \mathbf{Z}_ξ in the dimension of $N_s^\xi \times N_s^\xi$ are given by

$$\begin{aligned} \{\mathbf{V}_\xi\}_{(b,q,j)} &= \frac{1}{4\pi\sigma_1} \hat{\mathbf{n}}(\mathbf{r}_{(b,q,j)}) \\ &\cdot \left\{ \frac{\mathbf{q}}{|\mathbf{r}_{(b,q,j)} - \mathbf{r}_0|^3} - \frac{3[\mathbf{q} \cdot (\mathbf{r}_{(b,q,j)} - \mathbf{r}_0)](\mathbf{r}_{(b,q,j)} - \mathbf{r}_0)}{|\mathbf{r}_{(b,q,j)} - \mathbf{r}_0|^5} \right\} \end{aligned} \quad (20)$$

$$\begin{aligned} \{\mathbf{Z}_\xi\}_{(b,q,j)(a,p,i)} &= \frac{\sigma_j + \sigma_{j+1}}{2(\sigma_{j+1} - \sigma_j)} \vartheta^{-1}(\mathbf{r}_{(b,q,j)}) \delta_{ab} \delta_{pq} \delta_{ij} \\ &- \text{P.V.} \int_{\Delta_p^i} \partial_{\mathbf{n}} G(\mathbf{r}_{(b,q,j)}, \mathbf{r}') \vartheta^{-1}(\mathbf{r}') L_{(a,p,i)}(\mathbf{r}') d\mathbf{r}' \end{aligned} \quad (21)$$

where $N_s^\xi = N_a \sum_{i=1}^{N_i} N_p^i$. After the solution of (18) for \mathbf{I}_ξ , $V(\mathbf{r})$ at the arbitrary point \mathbf{r} can be obtained using (4) as

$$\begin{aligned} V(\mathbf{r}) &= \frac{V^{\text{inc}}(\mathbf{r})}{\sigma_1} + \sum_{i=1}^{N_i} \sum_{p=1}^{N_p^i} \sum_{a=1}^{N_a} \{\mathbf{I}_\xi\}_{(a,p,i)} \times \\ &\int_{\Delta_p^i} G(\mathbf{r}, \mathbf{r}') \vartheta^{-1}(\mathbf{r}') L_{(a,p,i)}(\mathbf{r}') d\mathbf{r}'. \end{aligned} \quad (22)$$

3) ISADL Formulation: For ISA for the DL approach, first, the unknown $V_{\text{ISA}}(\mathbf{r})$ at $\mathbf{r} \in S_1, \dots, S_{K-1}$ is expanded as

$$V_{\text{ISA}}(\mathbf{r}) = \sum_{i=1}^{K-1} \sum_{p=1}^{N_p^i} \sum_{a=1}^{N_a} \{\mathbf{I}_{\text{ISA}}\}_{(a,p,i)} \vartheta^{-1}(\mathbf{r}) L_{(a,p,i)}(\mathbf{r}). \quad (23)$$

Inserting (23) into (6) and point-testing the resulting equation at $\mathbf{r}_{(b,q,j)}$, $j = 1, 2, \dots, K-1$, $q = 1, 2, \dots, N_p^j$, $b = 1, 2, \dots, N_a$ yields the following matrix equation system

$$\mathbf{Z}_{\text{ISA}} \mathbf{I}_{\text{ISA}} = \mathbf{V}_{\text{ISA}} \quad (24)$$

where the entries of \mathbf{V}_{ISA} with the dimension of $N_s^{\text{ISA}} \times 1$ and \mathbf{Z}_{ISA} with the dimension of $N_s^{\text{ISA}} \times N_s^{\text{ISA}}$ are given by

$$\{\mathbf{V}_{\text{ISA}}\}_{(b,q,j)} = V^{\text{inc}}(\mathbf{r}_{(b,q,j)}) \quad (25)$$

$$\begin{aligned} \{\mathbf{Z}_{\text{ISA}}\}_{(b,q,j)(a,p,i)} &= \frac{\sigma_j + \sigma_{j+1}}{2} \vartheta^{-1}(\mathbf{r}_{(b,q,j)}) \delta_{ab} \delta_{pq} \delta_{ij} - \\ &(\tilde{\sigma}_{i+1} - \sigma_i) \text{P.V.} \int_{\Delta_p^i} \partial_{\mathbf{n}'} G(\mathbf{r}_{(b,q,j)}, \mathbf{r}') \vartheta^{-1}(\mathbf{r}') L_{(a,p,i)}(\mathbf{r}') d\mathbf{r}' \end{aligned} \quad (26)$$

where $\tilde{\sigma}_{i+1} = \sigma_{i+1}$ for $i = 1, 2, \dots, K-2$ and $\tilde{\sigma}_{i+1} = 0$ for $i = K-1$.

Then, the unknown $V_{\text{corr}}(\mathbf{r})$ at $\mathbf{r} \in S_1, \dots, S_{N_i}$ is written as

$$V_{\text{corr}}(\mathbf{r}) = \sum_{i=1}^{N_i} \sum_{p=1}^{N_p^i} \sum_{a=1}^{N_a} \{\mathbf{I}_{\text{corr}}\}_{(a,p,i)} \vartheta^{-1}(\mathbf{r}) L_{(a,p,i)}(\mathbf{r}). \quad (27)$$

Inserting (27) into (7) and point-testing the resulting equation at $\mathbf{r}_{(b,q,j)}$, $j = 1, 2, \dots, N_i$, $q = 1, 2, \dots, N_p^j$, $b = 1, 2, \dots, N_a$ yields the following matrix equation system

$$\mathbf{Z}_{\text{corr}} \mathbf{I}_{\text{corr}} = \mathbf{V}_{\text{corr}} \quad (28)$$

where the entries of \mathbf{V}_{corr} with the dimension of $N_s^{\text{corr}} \times 1$ and \mathbf{Z}_{corr} with the dimension of $N_s^{\text{corr}} \times N_s^{\text{corr}}$ are given by

$$\begin{aligned} \{\mathbf{V}_{\text{corr}}\}_{(b,q,j)} &= \\ &\begin{cases} \frac{\sigma_K}{\sigma_{K-1}} V^{\text{inc}}(\mathbf{r}_{(b,q,j)}) + \sum_{i=1}^{K-2} \frac{\sigma_K(\sigma_{i+1} - \sigma_i)}{\sigma_{K-1}} \times \\ \int_{S_i} \partial_{\mathbf{n}'} G(\mathbf{r}_{(b,q,j)}, \mathbf{r}') V_{\text{ISA}}(\mathbf{r}') d\mathbf{r}', & \text{if } j = K, K+1, \dots, N_i \\ \frac{\sigma_K}{\sigma_{K-1}} V^{\text{inc}}(\mathbf{r}_{(b,q,j)}) - \sigma_K V_{\text{ISA}}(\mathbf{r}_{(b,q,j)}) + \sum_{i=1}^{K-2} \frac{\sigma_K(\sigma_{i+1} - \sigma_i)}{\sigma_{K-1}} \\ \times \int_{S_i} \partial_{\mathbf{n}'} G(\mathbf{r}_{(b,q,j)}, \mathbf{r}') V_{\text{ISA}}(\mathbf{r}') d\mathbf{r}', & \text{if } j = K-1 \\ \frac{\sigma_K}{\sigma_{K-1}} V^{\text{inc}}(\mathbf{r}_{(b,q,j)}) - \frac{\sigma_K(\sigma_j + \sigma_{j+1})}{2\sigma_{K-1}} V_{\text{ISA}}(\mathbf{r}_{(b,q,j)}) + \sum_{i=1}^{K-2} \\ \frac{\sigma_K(\sigma_{i+1} - \sigma_i)}{\sigma_{K-1}} \text{P.V.} \int_{S_i} \partial_{\mathbf{n}'} G(\mathbf{r}_{(b,q,j)}, \mathbf{r}') V_{\text{ISA}}(\mathbf{r}') d\mathbf{r}', & \text{if } j = 1, \dots, K-2 \end{cases} \end{aligned} \quad (29)$$

$$\begin{aligned} \{\mathbf{Z}_{\text{corr}}\}_{(b,q,j)(a,p,i)} &= \frac{\sigma_j + \sigma_{j+1}}{2} \vartheta^{-1}(\mathbf{r}_{(b,q,j)}) \delta_{ab} \delta_{pq} \delta_{ij} - \\ &(\sigma_{i+1} - \sigma_i) \text{P.V.} \int_{\Delta_p^i} \partial_{\mathbf{n}'} G(\mathbf{r}_{(b,q,j)}, \mathbf{r}') \vartheta^{-1}(\mathbf{r}') L_{(a,p,i)}(\mathbf{r}') d\mathbf{r}'. \end{aligned} \quad (30)$$

After the solution of (24) and (28) for \mathbf{I}_{ISA} and \mathbf{I}_{corr} , respectively, $V(\mathbf{r})$ at \mathbf{r} on one patch of the interfaces S_1, S_2, \dots, S_{N_i} can be obtained using (5) as

$$V(\mathbf{r}) = \begin{cases} \sum_{a=1}^{N_a} \{\{\mathbf{I}_{\text{ISA}}\}_a + \{\mathbf{I}_{\text{corr}}\}_a\} \vartheta^{-1}(\mathbf{r}) L_a(\mathbf{r}), \\ \text{if } \mathbf{r} \in S_1, \dots, S_{K-1} \\ \sum_{a=1}^{N_a} \{\mathbf{I}_{\text{corr}}\}_a \vartheta^{-1}(\mathbf{r}) L_a(\mathbf{r}), \text{ if } \mathbf{r} \in S_K, \dots, S_{N_i} \end{cases} \quad (31)$$

4) IADL Formulation: For the IADL approach, the unknown $J_{N_i-1}(\mathbf{r})$ and $J_{N_i}(\mathbf{r})$ at $\mathbf{r} \in S_{N_i-1}$ and $\mathbf{r} \in S_{N_i}$ are expanded respectively as

$$J_{N_i-1}(\mathbf{r}) = \sum_{p=1}^{N_p^{N_i-1}} \sum_{a=1}^{N_a} \{\mathbf{I}_{N_i-1}\}_{(a,p,N_i-1)} \vartheta^{-1}(\mathbf{r}) L_{(a,p,N_i-1)}(\mathbf{r}) \quad (32)$$

$$J_{N_i}(\mathbf{r}) = \sum_{p=1}^{N_p^{N_i}} \sum_{a=1}^{N_a} \{\mathbf{I}_{N_i}\}_{(a,p,N_i)} \vartheta^{-1}(\mathbf{r}) L_{(a,p,N_i)}(\mathbf{r}). \quad (33)$$

Inserting (32)-(33) into (10)-(11) and point-testing the resulting equations at $\mathbf{r}_{(b,q,N_i-1)}$, $q = 1, 2, \dots, N_p^{N_i-1}$, $b = 1, 2, \dots, N_a$ and $\mathbf{r}_{(b,q,N_i)}$, $q = 1, 2, \dots, N_p^{N_i}$, $b = 1, 2, \dots, N_a$, respectively, yields the following matrix equation system

$$\begin{bmatrix} \mathbf{Z}_{N_i-1, N_i-1} & \mathbf{Z}_{N_i-1, N_i} \\ \mathbf{Z}_{N_i, N_i-1} & \mathbf{Z}_{N_i, N_i} \end{bmatrix} \begin{bmatrix} \mathbf{I}_{N_i-1} \\ \mathbf{I}_{N_i} \end{bmatrix} = \begin{bmatrix} \mathbf{V}_{N_i-1} \\ \mathbf{V}_{N_i} \end{bmatrix} \quad (34)$$

where the entries of \mathbf{V}_{N_i-1} with the dimension of $N_s^{N_i-1} \times 1$, \mathbf{V}_{N_i} with the dimension of $N_s^{N_i-1} \times 1$, $\mathbf{Z}_{N_i-1, N_i-1}$ with the dimension of $N_s^{N_i-1} \times N_s^{N_i-1}$, \mathbf{Z}_{N_i-1, N_i} with the dimension of $N_s^{N_i-1} \times N_s^{N_i}$, \mathbf{Z}_{N_i, N_i-1} with the dimension of $N_s^{N_i-1} \times N_s^{N_i}$, \mathbf{Z}_{N_i, N_i} with the dimension of $N_s^{N_i} \times N_s^{N_i}$

$N_s^{N_i} \times N_s^{N_i-1}$, and \mathbf{Z}_{N_i, N_i} with the dimension of $N_s^{N_i} \times N_s^{N_i}$ are given by

$$\{\mathbf{V}_{N_i-1}\}_{(b,q,N_i-1)} = \frac{\sigma_{N_i-1}}{\sigma_{N_i} - \sigma_{N_i-1}} \xi(\mathbf{r}_{(b,q,N_i-1)}) \quad (35)$$

$$\{\mathbf{V}_{N_i}\}_{(b,q,N_i)} = 0 \quad (36)$$

$$\begin{aligned} \{\mathbf{Z}_{N_i-1, N_i-1}\}_{(b,q,N_i-1)(a,p,N_i-1)} &= -\frac{1}{2} \vartheta^{-1}(\mathbf{r}_{(b,q,N_i-1)}) \delta_{ab} \delta_{pq} \\ &+ \text{P.V.} \int_{\Delta_p^{N_i-1}} \partial_{\mathbf{n}} G(\mathbf{r}_{(b,q,N_i-1)}, \mathbf{r}') \vartheta^{-1}(\mathbf{r}') L_{(a,p,N_i-1)}(\mathbf{r}') d\mathbf{r}' \end{aligned} \quad (37)$$

$$\begin{aligned} \{\mathbf{Z}_{N_i-1, N_i}\}_{(b,q,N_i-1)(a,p,N_i)} &= \\ &\int_{\Delta_p^{N_i}} \partial_{\mathbf{n}} G(\mathbf{r}_{(b,q,N_i-1)}, \mathbf{r}') \vartheta^{-1}(\mathbf{r}') L_{(a,p,N_i)}(\mathbf{r}') d\mathbf{r}' \end{aligned} \quad (38)$$

$$\begin{aligned} \{\mathbf{Z}_{N_i, N_i-1}\}_{(b,q,N_i)(a,p,N_i-1)} &= \\ &\int_{\Delta_p^{N_i-1}} \partial_{\mathbf{n}} G(\mathbf{r}_{(b,q,N_i)}, \mathbf{r}') \vartheta^{-1}(\mathbf{r}') L_{(a,p,N_i-1)}(\mathbf{r}') d\mathbf{r}' \end{aligned} \quad (39)$$

$$\begin{aligned} \{\mathbf{Z}_{N_i, N_i}\}_{(b,q,N_i)(a,p,N_i)} &= \frac{1}{2} \vartheta^{-1}(\mathbf{r}_{(b,q,N_i)}) \delta_{ab} \delta_{pq} + \\ &\text{P.V.} \int_{\Delta_p^{N_i}} \partial_{\mathbf{n}} G(\mathbf{r}_{(b,q,N_i)}, \mathbf{r}') \vartheta^{-1}(\mathbf{r}') L_{(a,p,N_i)}(\mathbf{r}') d\mathbf{r}' \end{aligned} \quad (40)$$

After the solution of (34) for \mathbf{I}_{N_i-1} and \mathbf{I}_{N_i} , $V(\mathbf{r})$ at $\mathbf{r} \in \Omega_{N_i}$ can be obtained using (9) as

$$\begin{aligned} V(\mathbf{r}) &= \sum_{p=1}^{N_p^{N_i-1}} \sum_{a=1}^{N_a} \{\mathbf{I}_{N_i-1}\}_{(a,p,N_i-1)} \times \\ &\int_{\Delta_p^{N_i-1}} G(\mathbf{r}, \mathbf{r}') \vartheta^{-1}(\mathbf{r}') L_{(a,p,N_i-1)}(\mathbf{r}') d\mathbf{r}' + \sum_{p=1}^{N_p^{N_i}} \sum_{a=1}^{N_a} \\ &\{\mathbf{I}_{N_i}\}_{(a,p,N_i)} \int_{\Delta_p^{N_i}} G(\mathbf{r}, \mathbf{r}') \vartheta^{-1}(\mathbf{r}') L_{(a,p,N_i)}(\mathbf{r}') d\mathbf{r}', \quad \mathbf{r} \in \Omega_{N_i} \end{aligned} \quad (41)$$

C. Numerical Evaluation of the Surface Integrals

As seen in (17), (21)-(22), (26), (29)-(30), and (37)-(41), there are three kinds of surface integrals as given by

$$I_1 = \int_{\Delta_p^i} \partial_{\mathbf{n}'} G(\mathbf{r}_{(b,q,j)}, \mathbf{r}') \vartheta^{-1}(\mathbf{r}') L_{(a,p,i)}(\mathbf{r}') d\mathbf{r}' \quad (42)$$

$$I_2 = \int_{\Delta_p^i} \partial_{\mathbf{n}} G(\mathbf{r}_{(b,q,j)}, \mathbf{r}') \vartheta^{-1}(\mathbf{r}') L_{(a,p,i)}(\mathbf{r}') d\mathbf{r}' \quad (43)$$

$$I_3 = \int_{\Delta_p^i} G(\mathbf{r}, \mathbf{r}') \vartheta^{-1}(\mathbf{r}') L_{(a,p,i)}(\mathbf{r}') d\mathbf{r}' \quad (44)$$

Depending on the distance d between the observation point ($\mathbf{r}_{(b,q,j)}$ or \mathbf{r}) and the source triangular patch Δ_p^i , three following cases are considered for the evaluation of the surface integrals I_1 , I_2 , and I_3 in (42)-(44).

1) Far-interaction: When the observation point ($\mathbf{r}_{(b,q,j)}$ or \mathbf{r}) is not located on the source triangular patch Δ_p^i and far away from Δ_p^i with the distance $d > \chi$, where χ is a threshold value, the surface integrals I_1 , I_2 , and I_3 in (42)-(44) can be calculated by first mapping the integrals in the Cartesian coordinate system to those in the parametric

coordinate system and then using the N_a -point Gaussian quadrature rule [30] for the numerical evaluation of them resulting in the expressions

$$\begin{aligned} I_1 &= \int_{\Delta_p^i} \partial_{\mathbf{n}'} G(\mathbf{r}_{(b,q,j)}, \mathbf{r}') \vartheta^{-1}(\mathbf{r}') L_{(a,p,i)}(\mathbf{r}') d\mathbf{r}' \\ &= \omega_{(a,p,i)} \hat{\mathbf{n}}'(\mathbf{r}'_{(a,p,i)}) \cdot \frac{\mathbf{r}_{(b,q,j)} - \mathbf{r}'_{(a,p,i)}}{8\pi |\mathbf{r}_{(b,q,j)} - \mathbf{r}'_{(a,p,i)}|^3} \end{aligned} \quad (45)$$

$$\begin{aligned} I_2 &= \int_{\Delta_p^i} \partial_{\mathbf{n}} G(\mathbf{r}_{(b,q,j)}, \mathbf{r}') \vartheta^{-1}(\mathbf{r}') L_{(a,p,i)}(\mathbf{r}') d\mathbf{r}' \\ &= \omega_{(a,p,i)} \hat{\mathbf{n}}(\mathbf{r}_{(b,q,j)}) \cdot \frac{\mathbf{r}'_{(a,p,i)} - \mathbf{r}_{(b,q,j)}}{8\pi |\mathbf{r}_{(b,q,j)} - \mathbf{r}'_{(a,p,i)}|^3} \end{aligned} \quad (46)$$

$$\begin{aligned} I_3 &= \int_{\Delta_p^i} G(\mathbf{r}, \mathbf{r}') \vartheta^{-1}(\mathbf{r}') L_{(a,p,i)}(\mathbf{r}') d\mathbf{r}' \\ &= \omega_{(a,p,i)} \frac{1}{8\pi |\mathbf{r} - \mathbf{r}'_{(a,p,i)}|} \end{aligned} \quad (47)$$

where $\mathbf{r}'_{(a,p,i)}$ is the source Gaussian quadrature point same as the a th interpolation point on the p th patch of the i th interface, and $\omega_{(a,p,i)}$ is the weight coefficient associated with $\mathbf{r}'_{(a,p,i)}$.

Clearly, the computation of I_1 , I_2 , and I_3 is simplified for the far-interaction case due to the flexibility of the choice of the interpolation points using the proposed scheme.

2) Near-interaction: When the observation point ($\mathbf{r}_{(b,q,j)}$ or \mathbf{r}) is not located on Δ_p^i and close to Δ_p^i with the distance $d < \chi$, after the space mapping from the Cartesian coordinate system to the parametric coordinate system for the surface integrals I_1 , I_2 , and I_3 in (42)-(44), we can use the N_k -point Gaussian quadrature rule [30] for the numerical evaluation of them resulting in the following expressions

$$\begin{aligned} I_1 &= \int_{\Delta_p^i} \partial_{\mathbf{n}'} G(\mathbf{r}_{(b,q,j)}, \mathbf{r}') \vartheta^{-1}(\mathbf{r}') L_{(a,p,i)}(\mathbf{r}') d\mathbf{r}' \\ &= \sum_{k=1}^{N_k} \omega_k L_{(a,p,i)}(\mathbf{r}'_k) \hat{\mathbf{n}}'(\mathbf{r}'_k) \cdot \frac{\mathbf{r}_{(b,q,j)} - \mathbf{r}'_k}{8\pi |\mathbf{r}_{(b,q,j)} - \mathbf{r}'_k|^3} \end{aligned} \quad (48)$$

$$\begin{aligned} I_2 &= \int_{\Delta_p^i} \partial_{\mathbf{n}} G(\mathbf{r}_{(b,q,j)}, \mathbf{r}') \vartheta^{-1}(\mathbf{r}') L_{(a,p,i)}(\mathbf{r}') d\mathbf{r}' \\ &= \sum_{k=1}^{N_k} \omega_k L_{(a,p,i)}(\mathbf{r}'_k) \hat{\mathbf{n}}(\mathbf{r}_{(b,q,j)}) \cdot \frac{\mathbf{r}'_k - \mathbf{r}_{(b,q,j)}}{8\pi |\mathbf{r}_{(b,q,j)} - \mathbf{r}'_k|^3} \end{aligned} \quad (49)$$

$$\begin{aligned} I_3 &= \int_{\Delta_p^i} G(\mathbf{r}, \mathbf{r}') \vartheta^{-1}(\mathbf{r}') L_{(a,p,i)}(\mathbf{r}') d\mathbf{r}' \\ &= \sum_{k=1}^{N_k} \omega_k L_{(a,p,i)}(\mathbf{r}'_k) \frac{1}{8\pi |\mathbf{r} - \mathbf{r}'_k|} \end{aligned} \quad (50)$$

where $N_k > N_a$, \mathbf{r}'_k is the k th source Gaussian quadrature point, and ω_k is the weight coefficient associated with \mathbf{r}'_k .

3) Self-interaction: When the observation point ($\mathbf{r}_{(b,q,j)}$ or \mathbf{r}) is located on Δ_p^i , the integrands of the surface integrals I_1 , I_2 , and I_3 in (42)-(44) become singular. For this case, direct numerical evaluation of them can not be used anymore due to the large numerical error. Therefore,

techniques for the singularity treatment should be applied. Specifically, the integrands of I_2 in (43) and I_3 in (44) become weakly-singular while that of I_1 in (42) becomes strongly-singular for the self interaction case. The weakly-singular surface integrals I_2 in (43) and I_3 in (44) can be evaluated using the Duffy method [31] while the strongly-singular surface integral I_1 in (42) can be evaluated using the polar coordinate transformation method [27], [32]. It should be noted that, the implementations of both the Duffy and polar coordinate transformation methods still require the numerical evaluation of line integrals, which can be addressed using the N_v -point Gauss-Legendre quadrature rule [30]. For the details of the implementations of the weakly- and strongly-singularity treatment techniques, interested readers can be referred to [27], [31], [32].

III. Numerical Results

In this section, numerical experiments are presented to demonstrate the accuracy, flexibility, and efficiency of the proposed scheme for SIEs for analyzing the EEG forward problem.

A spherical head volume conductor model is considered in this section since the electric potential on the exterior surface of the spherical head model can be analytically obtained as the reference solution [33]. We consider a spherical head model composed of three layers (i.e., $N_i = 3$) representing the brain, skull, and scalp tissues from the inner to the outer, respectively. The radii of the spherical interfaces S_1 , S_2 , and S_3 are 0.087, 0.092, and 0.1 m, respectively. The dipolar moment is $\mathbf{q} = (1, 0, 1)/\sqrt{2}$ A · m.

To quantify the accuracy of the solution of SIEs, the relative error of the solution is defined by comparing the electric potential on S_3 obtained after using the proposed scheme with the analytical reference solution [33] as

$$\text{Relative error} = \sqrt{\frac{\sum_{p=1}^{N_p^3} |\tilde{V}^{\text{ref}}(\mathbf{r}_p^c) - \tilde{V}^{\text{num}}(\mathbf{r}_p^c)|^2}{\sum_{p=1}^{N_p^3} |\tilde{V}^{\text{ref}}(\mathbf{r}_p^c)|^2}} \quad (51)$$

where \mathbf{r}_p^c denotes the center point of the p th quadratically curved triangular patch on S_3 , “ref” denotes the analytical reference solution [33], “num” denotes the numerical solution obtained after using the proposed scheme, and $\tilde{V}^{\text{type}}(\mathbf{r}_p^c)$, $\text{type} \in \{\text{ref}, \text{num}\}$ is defined as

$$\tilde{V}^{\text{type}}(\mathbf{r}_p^c) = V^{\text{type}}(\mathbf{r}_p^c) - \frac{\sum_{q=1}^{N_p^3} V^{\text{type}}(\mathbf{r}_q^c)}{N_p^3}. \quad (52)$$

Note that, using $\tilde{V}^{\text{type}}(\mathbf{r}_p^c)$ for the computation of the relative error in (51) ensures that both the analytical and numerical solutions have zero means prior to the comparison [12].

Unless stated otherwise in this section, for the numerical evaluation of the surface integrals in Section II-C, the distance threshold value is set to be $\chi = 0.04$ m, the 16-point Gaussian quadrature rule is used for the surface

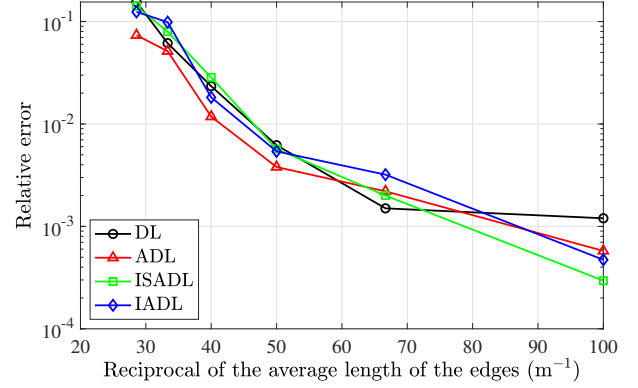


Fig. 4. The relative error of the solution after using the proposed scheme versus the reciprocal of the average length of the edges for the DL, ADL, ISADL, and IADL approaches.

integrals for the near interaction (i.e., $N_k = 16$), and the 15-point Gauss-Legendre quadrature rule is used for the line integrals for the self interaction (i.e., $N_v = 15$). A LU decomposition-based direct solver [34] is used for solving the matrix equation systems in Section II-B.

As the first numerical experiment, the effect of the mesh density on the accuracy of the solution of SIEs using the proposed scheme is investigated. The dipolar source is located at $\mathbf{r}_0 = (0.0425, 0, 0)$ m. The conductivities of three layers are $\sigma_1 = 1$ S/m, $\sigma_2 = 0.025$ S/m, and $\sigma_3 = 1$ S/m, respectively. The 2th order interpolation function is used for the Nyström method (i.e., $N_a = 6$). Six sets of the mesh density are considered as $h = \{0.01, 0.015, 0.02, 0.025, 0.03, 0.035\}$ m resulting in $N_p^1 = \{1918, 854, 456, 300, 208, 136\}$, $N_p^2 = \{2170, 932, 532, 326, 214, 172\}$, and $N_p^3 = \{2556, 1120, 626, 400, 282, 202\}$, respectively.

Fig. 4 plots the relative error of the solution after using the proposed scheme versus the reciprocal of the average length of the edges for the DL, ADL, ISADL, and IADL approaches. As seen from this figure, the relative error of the solution after using the proposed scheme decreases with the increase of the mesh density for all the four approaches, which demonstrate the efficiency of the proposed scheme. In addition, the ISADL approach has the smallest relative error of the solution for all the six sets of the mesh density among all the four approaches.

For the second numerical experiment, we investigate the effect of the order of the interpolation function on the accuracy of the solution of SIEs using the proposed scheme. The dipolar source is located at $\mathbf{r}_0 = (0.0425, 0, 0)$ m. The conductivities of three layers are $\sigma_1 = 1$ S/m, $\sigma_2 = 0.025$ S/m, and $\sigma_3 = 1$ S/m, respectively. The average edge length of the mesh is $h = 0.01$ m resulting in $N_p^1 = 1918$, $N_p^2 = 2170$, and $N_p^3 = 2556$. Three sets of the interpolation function are considered as order = {0, 1, 2}th for the Nyström method, i.e., $N_a = \{1, 3, 6\}$, respectively.

Fig. 5 compares the relative error of the solution after using the proposed scheme versus the order of the interpolation function for the DL, ADL, ISADL, and IADL approaches. This figure shows that the accuracy

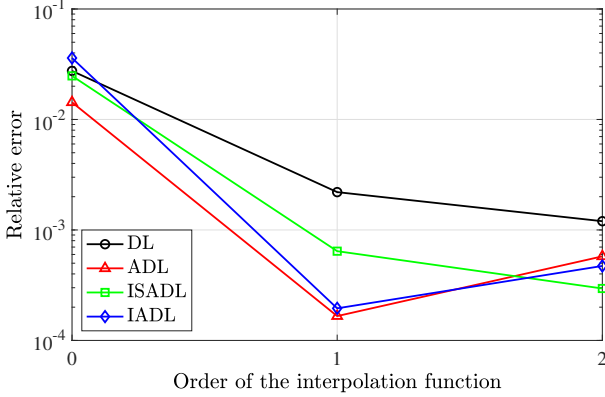


Fig. 5. The relative error of the solution after using the proposed scheme versus the order of the interpolation function for the DL, ADL, ISADL, and IADL approaches.

of the solution of SIEs using the proposed scheme for all the four approaches is satisfactory for most applications. Additionally, the relative error of the solution after using the proposed scheme decreases with the increase of the order of the interpolation function for all the approaches except for the ADL and IADL approaches. These observations demonstrate the flexibility of the proposed scheme while the saturation behavior of the plots for the ADL and IADL approaches is due to the fact that the accuracy of the mesh used for this experiment is limited for these two approaches for the 2nd order interpolation function. Note that similar saturation behaviors appear in other references [23], [25] using the Nyström-based HO discretization methods. The usage of higher-order surface patches (e.g., cubic) could be helpful to alleviate the saturation issue, which is out of the scope of this paper.

Next, the effect of the dipole position on the accuracy of the solution of SIEs using the proposed scheme is investigated. The 2th order interpolation function is used for the Nyström method (i.e., $N_a = 6$). The mesh density is $h = 0.02$ m resulting in $N_p^1 = 456$, $N_p^2 = 532$, and $N_p^3 = 626$. Twelve sets of the dipole position located along the x -axis are considered as $\mathbf{r}_0 = (x_0, 0, 0)$ m with $x_0 = \{0.1, 1, 2, 3, 4.25, 5, 6, 7, 7.5, 8, 8.25, 8.4\} \times 10^{-2}$.

Fig. 6 shows the relative error of the solution after using the proposed scheme versus the dipole position for the DL, ADL, ISADL, and IADL approaches. As we can see from the figure, the accuracy of the solution of SIEs using the proposed scheme for all the four approaches is good when $x_0 \leq 0.075$ while it becomes worse as the dipolar source approaches the boundary of the interior layer S_1 . This behavior observed from Fig. 6 matches with that observed from Fig. 4 in [12] and Fig. 6 in [18].

As the last numerical experiment, the effect of the conductivity of the skull layer on the accuracy of the solution of SIEs using the proposed scheme is investigated. The dipolar source is located at $\mathbf{r}_0 = (0.0425, 0, 0)$ m. The 2nd order interpolation function is used for the Nyström method (i.e., $N_a = 6$). The mesh density is $h = 0.02$ m resulting in $N_p^1 = 456$, $N_p^2 = 532$, and $N_p^3 = 626$. The

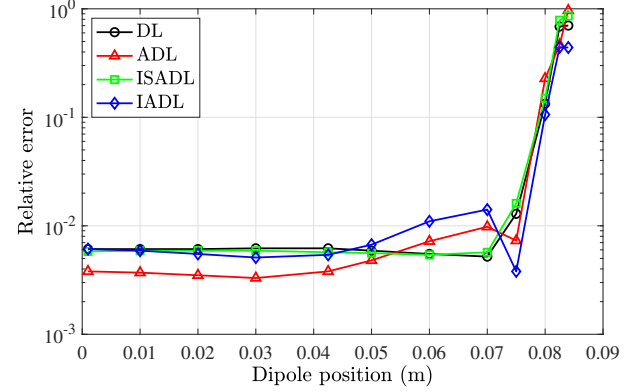


Fig. 6. The relative error of the solution after using the proposed scheme versus the dipole position for the DL, ADL, ISADL, and IADL approaches.

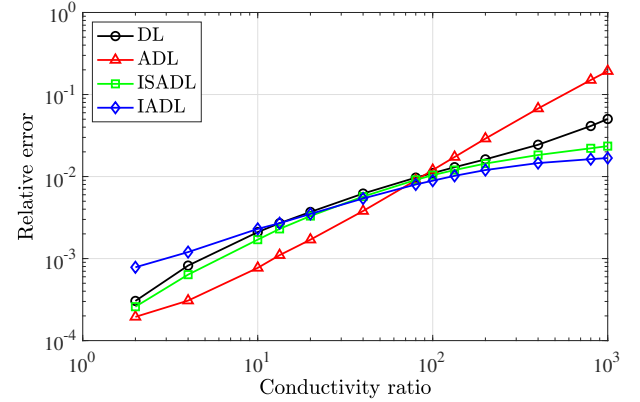


Fig. 7. The relative error of the solution after using the proposed scheme versus the conductivity ratio for the DL, ADL, ISADL, and IADL approaches.

conductivities of the inner and outer layers are $\sigma_1 = 1$ S/m and $\sigma_3 = 1$ S/m, respectively. Thirteen sets of the conductivities of the middle layer are considered as $\sigma_2 = \{50, 25, 10, 7.5, 5, 2.5, 1.25, 10, 0.75, 0.5, 0.25, 0.125, 0.1\} \times 10^{-2}$ S/m, i.e., the ratio of the conductivities between the brain/scalp layer and the skull layer is $\{2, 4, 10, 13.33, 20, 40, 80, 100, 133.33, 200, 400, 800, 1000\}$, which covers the usual range of the conductivity ratio [35].

Fig. 7 compares the relative error of the solution after using the proposed scheme versus the conductivity ratio for the DL, ADL, ISADL, and IADL approaches. This figure shows that, the relative error of the solution after using the proposed scheme for all the approaches increases with the decrease of σ_2 , which is due to the isolated skull problem [16]. However, due to the improvement of the SIE formulation, the ISADL approach is more resistant to the increase of the conductivity ratio than the DL approach. Moreover, the IADL approach has the best accuracy among all the four approaches for large conductivity ratios, which matches with the behavior observed from Fig. 8 in [18]. Clearly, these results demonstrate the efficiency of the proposed scheme for discretizing SIEs for all the four approaches.

IV. Conclusion

In this work we propose a Nyström-based HO discretization scheme for SIEs for analyzing the EEG forward problem. The HO surface elements and the HO basis functions are used for the discretization of the interfaces of the head volume and the unknowns on the elements, respectively. Differently from existing works using the isoparametric HO discretization scheme, this work employs interpolation points different from the mesh nodes, which allows for the flexible manipulation of the order of the basis functions without the requirement of the regeneration of the mesh of the interfaces. In addition, since the interpolation points are the same as the Gaussian quadrature points on the elements, the numerical computation of the surface integrals is simplified for the far-interaction case. Several numerical experiments are presented to demonstrate the accuracy, flexibility, and efficiency of the proposed discretization scheme for the DL, ADL, ISADL, and IADL approaches for analyzing the EEG forward problem.

The development of the Nyström-based HO discretization scheme for the symmetric SIE [12] for analyzing the EEG forward problem is undergoing, which needs the treatment of the hyper-singularity for the self-interaction case, and it will be presented in our future work.

References

- [1] R. Cabeza and A. Kingstone, *Handbook of Functional Neuroimaging of Cognition*. Cambridge, MA, USA: MIT Press, Second Edition, May 2006.
- [2] Z. A. Acar, C. E. Acar, and S. Makeig, “Simultaneous head tissue conductivity and EEG source location estimation,” *NeuroImage*, vol. 124, pp. 168–180, 2016.
- [3] C. Phillips, M. D. Rugg, and K. J. Friston, “Systematic regularization of linear inverse solutions of the EEG source localization problem,” *NeuroImage*, vol. 17, no. 1, pp. 287–301, 2002.
- [4] R. D. P.-Marqui, “Review of methods for solving the EEG inverse problem,” *Int. J. Bioelectromagn.*, vol. 1, no. 1, pp. 75–86, 1999.
- [5] Z. A. Acar and S. Makeig, “Effects of forward model errors on EEG source localization,” *Brain Topogr.*, vol. 26, no. 3, pp. 378–396, 2013.
- [6] K. A. Awada, D. R. Jackson, J. T. Williams, D. R. Wilton, S. B. Baumann, A. C. Papanicolaou, “Computational aspects of finite element modeling in EEG source localization,” *IEEE Trans. Biomed. Eng.*, vol. 44, no. 8, pp. 736–752, 1997.
- [7] M. C. Piastra, A. Nüßing, J. Vorwerk, H. Bornfleth, R. Oostenveld, C. Engwer, and C. H. Wolters, “The discontinuous Galerkin finite element method for solving the MEG and the combined MEG/EEG forward problem,” *Frontiers Neurosci.*, vol. 12, pp. 30, Feb. 2018.
- [8] J. Vorwerk, C. Engwer, S. Pursiainen, and C. H. Wolters, “A mixed finite element method to solve the EEG forward problem,” *IEEE Trans. Med. Imag.*, vol. 36, no. 4, pp. 930–941, Apr. 2017.
- [9] N. Yavich, N. Koshev, M. Malovichko, A. Razorenova, and M. Fedorov, “Conservative finite element modeling of EEG and MEG on unstructured grids,” *IEEE Trans. Med. Imag.*, vol. 41, no. 3, pp. 647–656, Mar. 2022.
- [10] B. He, T. Misha, Y. Okamoto, S. Homma, Y. Nakajima, and T. Sato, “Electric dipole tracing in the brain by means of the boundary element method and its accuracy,” *IEEE Trans. Biomed. Eng.*, vol. 6, pp. 406–414, 1987.
- [11] H. Hallez, et al., “Review on solving the forward problem in EEG source analysis,” *J. NeuroEng. Rehabil.*, vol. 4, no. 1, pp. 46, 2007.
- [12] J. Kybic, M. Clerc, T. Abboud, O. Faugeras, R. Keriven, T. Papadopoulou, “A common formalism for the integral formulations of the forward EEG problem,” *IEEE Trans. Med. Imaging*, vol. 24, no. 1, pp. 12–28, 2005.
- [13] J. W. H. Meijis, O. W. Weier, M. J. Peters, and A. van Oosterom, “On the numerical accuracy of the boundary element method,” *IEEE Trans. Biomed. Eng.*, vol. 36, pp. 1038–1049, 1989.
- [14] J. C. de Munck, “A linear discretization of the volume conductor boundary integral equation using analytically integrated elements,” *IEEE Trans. Biomed. Eng.*, vol. 39, pp. 986–990, 1992.
- [15] H. A. Schlitt, L. Heller, R. Aaron, E. Best, and D. M. Ranken, “Evaluation of boundary element methods for the EEG forward problem: Effect of linear interpolation,” *IEEE Trans. Biomed. Eng.*, vol. 42, pp. 52–58, 1995.
- [16] M. S. Hamalainen and J. Sarvas, “Realistic conductivity geometry model of the human head for interpretation of neuromagnetic data,” *IEEE Trans. Biomed. Eng.*, vol. 36, no. 2, pp. 165–171, 1989.
- [17] V. Giunzioni, J. E. Ortiz G., A. Merlini, S. B. Adrian, and F. P. Andriulli, “On a Calderón preconditioner for the symmetric formulation of the electroencephalography forward problem without barycentric refinements,” *J. Computat. Phys.*, vol. 491, pp. 112374, 2023.
- [18] L. Rahmouni, S. B. Adrian, K. Cools, and F. P. Andriulli, “Conforming discretizations of boundary element solutions to the electroencephalography forward problem,” *C. R. Physique*, vol. 19, pp. 7–25, 2018.
- [19] M. Y. Monin, L. Rahmouni, A. Merlini, and F. P. Andriulli, “A hybrid volume-surface-wire integral equation for the anisotropic forward problem in electroencephalography,” *IEEE J. Electromagn., RF, Microw. Med. Biol.*, vol. 4, no. 4, pp. 286–293, Dec. 2020.
- [20] J. H. M. Frijns, S. L. de Snoo, and R. Schoonhoven, “Improving the accuracy of the boundary element method by the use of second-order interpolation functions,” *IEEE Trans. Biomed. Eng.*, vol. 47, no. 10, pp. 1336–1346, 2000.
- [21] N. G. Gençer and I. O. Tanzer, “Forward problem solution of electromagnetic source imaging using a new BEM formulation with high-order elements,” *Phys. Med. Biol.*, vol. 44, pp. 2275–2287, 1999.
- [22] N. G. Gençer and Z. A.-Acar, “Use of the isolated problem approach for multi-compartment BEM models of electro-magnetic source imaging,” *Phys. Med. Biol.*, vol. 50, pp. 3007–3022, 2005.
- [23] G. Kang, J. Song, W. C. Chew, K. C. Donepudi, and J.-M. Jin, “A novel grid-robust higher order vector basis function for the method of moments,” *IEEE Trans. Antennas Propag.*, vol. 49, no. 1, pp. 908–915, 2001.
- [24] R. Chen, S. B. Sayed, H. A. Ulku, and H. Bagci, “An explicit time marching scheme for efficient solution of the magnetic field integral equation at low frequencies,” *IEEE Trans. Antennas Propag.*, vol. 69, no. 2, pp. 1213–1218, 2021.
- [25] R. Chen and H. Bagci, “On higher-order Nyström discretization of scalar potential integral equation for penetrable scatterers,” in *Proceedings of the Applied Computational Electromagnetics Society Symposium*, Miami, FL, USA, 2019, pp. 1–2.
- [26] L. S. Canino, J. J. Ottusch, M. A. Stalzer, J. L. Visher, and S. Wandzura, “Numerical solution of the Helmholtz equation in 2D and 3D using a high-order Nyström discretization,” *J. Comput. Phys.*, vol. 146, pp. 627–633, 1998.
- [27] R. Chen, S. B. Sayed, N. Alharthi, D. Keyes, and H. Bagci, “An explicit marching-on-in-time scheme for solving the time domain Kirchhoff integral equation,” *J. Acoust. Soc. Am.*, vol. 146, no. 3, pp. 2068–2079, 2019.
- [28] R. Chen, Y. Shi, S. B. Sayed, M. Lu, and H. Bagci, “On the spurious resonance modes of time domain integral equations for analyzing acoustic scattering from penetrable objects,” *J. Acoust. Soc. Am.*, vol. 151, no. 2, pp. 1064–1076, 2022.
- [29] R. Chen, M. Li, and D. Ding, “A higher-order BEM discretization scheme for the EEG forward problem,” in *Proc. Photonics and Electromagnetics Research Symposium*, Chengdu, China, 2024, pp. 1–3.
- [30] J.-M. Jin, *Theory and Computation of Electromagnetic Fields*. Wiley, Hoboken, NJ, 2010.
- [31] M. G. Duffy, “Quadrature over a pyramid or cube of integrands with a singularity at a vertex,” *SIAM J. Numer. Anal.*, vol. 19, no. 6, pp. 1260–1262, 1982.
- [32] M. Guiggiani, G. Krishnasamy, T. J. Rudolphi, and F. Rizzo, “A general algorithm for the numerical solution of hypersingular boundary integral equations,” *J. Appl. Mech.*, vol. 59, no. 3, pp. 604–614, 1992.

- [33] Z. Zhang, "A fast method to compute surface potentials generated by dipoles within multilayer anisotropic spheres," *Phys. Med. Biol.*, vol. 40, pp. 335–349, 1995.
- [34] E. Anderson, Z. Bai, C. Bischof, L. S. Blackford, J. Demmel, J. Dongarra, J. Du Croz, A. Greenbaum, S. Hammarling, A. McKenney, and D. Sorensen, *LAPACK Users' Guide*. SIAM, Warrendale, PA, 1999.
- [35] S. I. Goncalves, J. C. D. Munck, J. P. A. Verbunt, F. Bijma, R. M. Heethaar, and F. L. D. Silva, "In vivo measurement of the brain and skull resistivities using an EIT-based method and realistic models for the head," *IEEE Trans. Biomed. Eng.*, vol. 50, no. 6, pp. 754–767, Jun. 2003.